Journal of Power Sources 196 (2011) 8525–8530

Contents lists available at ScienceDirect

Journal of Power Sources

journal homepage: www.elsevier.com/locate/jpowsour

Bi-modal water transport behavior across a simple Nafion membrane

Ziheng Zhang[a,1], Keith Promislow[b], Jonathan Martin[c], Haijiang Wang[c], Bruce J. Balcom[a,*]

[a] MRI Centre, Department of Physics, University of New Brunswick, Fredericton, New Brunswick, Canada E3B 5A3
[b] Department of Mathematics, Michigan State University, East Lansing, MI 48824, USA
[c] Institute for Fuel Cell Innovation (IFCI), National Research Council Canada (NRC), 4250 Wesbrook Mall, Vancouver, BC, Canada V6T 1W5

ARTICLE INFO

Article history:
Received 9 June 2011
Accepted 10 June 2011
Available online 22 June 2011

Keywords:
PEM fuel cell
Water management
Nafion
Mathematical model
Nuclear magnetic resonance imaging
MRI

ABSTRACT

The development of predictive mathematical models for water management in polymer electrolyte membrane fuel cells requires detailed understanding of water distribution and water transport across the Nafion layer. The anisotropic microstructure of Nafion suggests the measurement of water content and mass transport should be along the fuel cell functional direction, i.e. across the membrane. Non-invasive, high resolution, microscopy measurements of this type are very challenging.

We report here the calibration of a minimal mathematical model for diffusive water transport in Nafion against data from high-resolution water content maps determined with a new magnetic resonance imaging methodology developed for this purpose. A mock fuel cell was designed to permit well-controlled wetting and drying boundary conditions. With no chemical potential driving force involved, we assume the water transport behavior will be dominated by diffusion. Moreover we show that, in this context, our model is mathematically equivalent to the traditional permeation models based upon saturation dependent pressure gradients via a capillary pressure ansatz.

The non-linear equilibrium water distribution across the Nafion membrane measured in this work suggests a bi-modal diffusivity. The model constructed associates distinct transport behaviors to water contents above and below a critical threshold, consistent with a rearrangement of a micro-structural pore network. The experimental observation and the model prediction agree with the primary features of Weber's model of Nafion, which predicts distinct modes of transport for hydration fronts traversing the through-plane direction of the membrane.

© 2011 Published by Elsevier B.V.

1. Introduction

Polymer electrolyte membrane (PEM) fuel cells, as power conversion engines, generate useful voltage from electrochemical energy for automotive and stationary power applications with high efficiency and benign emissions [1–3]. The heart of PEM fuel cells is the organic polymer electrolyte membrane, e.g. Nafion, functioning simultaneously as an electrolyte conductor and a gas separator. The efficiency of polymer electrolyte membranes for fuel cell applications is dictated by the proton conductivity, which is determined by the proton mobility and proton concentration in the aqueous phase of the membrane [1].

Water management, maintaining an appropriate water balance within the membrane through control of the relative humidity (RH) of the input reactant gases, is critical to ensuring optimal operation of the PEM fuel cell [4,5]. Excess water produced in PEM fuel cells at the cathode can limit reactant gas transport. Too little water at the anode can cause the membrane to dry out and lose its conductivity. Reliable water management requires a detailed understanding of the transport mechanisms of water through the Nafion, which are still not well established.

Many models propose diffusion as the basic transport mechanism for water in Nafion [4], while others suggest hydraulic permeation [6–10]. Many current modeling efforts suppose a single-mode transport mechanism for water through the Nafion, and hence predict a smooth water distribution across the membrane. However, recent experimental evidence shows that a dry anode can be maintained while the wetter cathode has liquid water present during the fuel cell operation [1,9].

Moreover, Weber et al. [11,12] have proposed a model that proposes various transport modes based upon pore-expansion due to liquid pressure in connective nanopores within the ionomer. Depending upon the saturation level, their model has co-existing diffusive and permeation-based transport. In contrast to other theories, this model incorporates a degenerate transport mechanism, which indicates distinct transitions in water profiles without large fluxes [11,12].

* Corresponding author. Tel.: +1 506 458 7938; fax: +1 506 453 4581.
E-mail address: bjb@unb.ca (B.J. Balcom).
[1] Current address: Department of Diagnostic Radiology, Yale University School of Medicine, PO Box 208043, New Haven, CT 06520-8043, USA.

0378-7753/$ – see front matter © 2011 Published by Elsevier B.V.
doi:10.1016/j.jpowsour.2011.06.046

In an operating fuel cell, the proton conductivity, water diffusion coefficient, and electro-osmotic drag coefficient all vary as functions of water content in the membrane [13]. Direct measurements of water content in Nafion are hence of great importance in developing appropriate mathematical models, and many related studies have been reported in the last decade [14]. However, the anisotropic microstructure of Nafion [15–17] suggests the importance of measurements of water content along the cell's functional direction, i.e. across the membrane, which is distinct from information gathered from lengthwise measurements [18].

At present, optical visualization [19–23], neutron beam absorption [24–29], and magnetic resonance imaging [13,30–34] are three major non-invasive techniques utilized to monitor the water content variation inside PEM fuel cells. Optical methods depend on the transparency of the detecting materials. However, Nafion is semi-transparent, and will not permit quantitative water measurements as a function of depth across the membrane. Neutron beam methods feature a high sensitivity to water content; however they suffer from poor spatial resolution and difficulty with coordinate registration.

Magnetic resonance imaging is a promising technique with the potential for high resolution measurement [35–39]. From the literature, the majority of MRI approaches to this problem are based on frequency encoding spin echo techniques, which are highly sensitive to the local magnetic susceptibility variation and often yield images with artifacts. In general, removing these image artifacts requires a wide bandwidth signal which leads to a decreased signal to noise ratio (SNR) [33]. Moreover, the inherent signal contrast, which depends on the spin–spin relaxation time, T_2, renders the frequency encoded images non-quantitative, unless T_2 mapping is undertaken [38,39].

In this study, we report the measurement of the water content distribution across a Nafion 1110 membrane in a mock fuel cell, purposely designed to study water content variation across a Nafion membrane with one side equilibrated by liquid water and the other exposed to water vapor at well controlled RH. In the absence of the chemical reactions present in an operational fuel cell, our experimental set-up eliminates the electromotive driving force for proton transfer, and focuses on water transport issues. The results reveal a surprising family of quasi-equilibria of water distributions. In each time resolved image, the water content profile through the water equilibrated side of the Nafion is relatively flat, with a slight downward tilt toward the vapor equilibrated side, however at a critical value of the water content the slope of the water profile increases significantly. We attribute this non-uniform behavior to a phase-transition in the microstructure of the underlying water network [40].

This observation is similar to the observation of wet-cathode/dry-anode steady state in an operating fuel cell reported in several previous studies, which cannot be well described by non-degenerate transport models [41,42]. In this study, motivated by a reduction of the Weber–Newman model, we propose a minimal model for water transport, using a self-diffusivity for water that depends sensitively upon water concentration at a particular threshold. This model describes steady state behavior, with slow-relaxation or aging effects ignored.

The quantitatively excellent agreement between the experimental measurements and the model results support the idea of bifurcation in water network structure, as parameterized by average water content, leading to a bi-modal water transport mechanism. Moreover the transition threshold of our calibrated model is in excellent agreement of the liquid–vapor/vapor phase transition predicted by the Weber–Newman model.

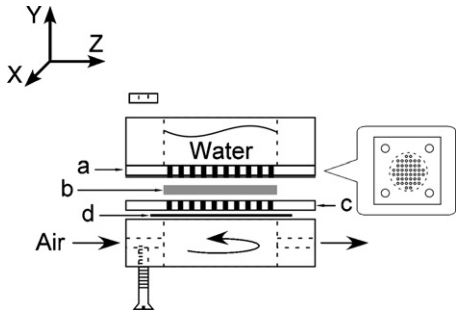

Fig. 1. Schematic of the mock fuel cell with wetting and drying boundary conditions. The Nafion layer (b) is held between two perforated plates (a, c), whose structure is illustrated in the inset at right. Plate (a) is fabricated from copper plated PC board. Plate (c) is made of G10 fiberglass. A water reservoir sits on top of plate (a) with a drying chamber underneath plate (c), also made from G10 fiberglass. Beneath plate (c), a circular RF coil with 1.8 cm diameter (d) was installed. The entire apparatus was held together by 4 brass screws with a controlled torque applied.

2. Experimental

2.1. Mock fuel cell

As shown in Fig. 1, the mock fuel cell chamber, 3 cm × 3 cm, was shaped from G10 fiberglass (McMaster-Carr, Cleveland, OH). The water reservoir on top of the Nafion layer saturates the sample, when desired, to ensure a fully wet boundary condition. On the other side, the gas chamber underneath maintains a constant drying boundary condition through a dry air flow, with the RH 12%. A perforated PC board between the reservoir and membrane was employed to remove the signal from the water reservoir through RF screening [38].

All perforated plates were 1.65 mm in thickness. The water reservoir and gas chamber frame were 6.35 mm thick. The assembly was embedded in a 1 cm thick Teflon sheet and placed in a copper covered Plexiglas tube.

2.2. Sample preparation

The sample film, Nafion 1110, 250 μm thick, was purchased from Ion Power (New Castle, DE). The Nafion 1110 was cut to a 2 cm diameter circle, and pretreated by heating in 3–5 wt.% H_2O_2 solution at 80 °C for 1 h. The sample was then rinsed in deionized water at 80 °C for 1 h, then, heated in 0.5 M H_2SO_4 at 80 °C for 1 h. The sample has finally cleaned by prolonged heating in deionized water at 80 °C for 1 h, to remove any possible chemical residues. The basic procedure was based on the work of Jalani [43] and Moore [44].

2.3. Magnetic resonance imaging

The ^{1}H magnetic resonance imaging measurements were implemented on a 2.4 T (100 MHz) horizontal bore superconducting magnet, with a Tecmag Apollo as the imaging console [38]. The RF probe was a custom built single channel surface coil. The RF resonator was formed from copper tape, cut into a circular shape, 2 cm in diameter, affixed to the surface of the gas chamber, shown in Fig. 1. The RF resonator was tuned to 100 MHz with two capacitors in a standard series–parallel tank circuit.

A specially developed MRI technique for thin film depth imaging, Double Half K-space Spin Echo Single Point Imaging (DHK SE SPI) [37], was employed to obtain 1D water content profiles. As a pure phase encoding measurement, it minimizes the potential image distortion from conductive materials in a fuel cell [45,46].

From previous studies [38,39], it is well known that the water T_2 in Nafion varies with the water content and pore level microstructure.

The MRI measurement averages the cross section of the sample while encoding along the depth direction y [38]. The spatially resolved image intensity is simply,

$$S(y) = \rho_0(y) \cdot \exp\left(-\frac{nTE}{T_2(y)}\right) \quad (1)$$

where n is the echo number, and TE is the echo time. $S(y)$ is the image intensity defined by the product of the water content, $\rho_0(y)$, and T_2 weighting in the exponential term.

The MRI measurement simultaneously maps T_2, permitting one to directly determine water content variation. By fitting each pixel in the profile series to Eq. (1), it is possible to separate the spatially resolved T_2 and the local ^{1}H density, $\rho_0(y)$, corresponding to the water content. From previous studies [38,39], the water T_2 in Nafion exhibits a single exponential decay, which is assumed in the T_2 fitting for all measurements in the current study.

The nominal resolution of the images, and the resultant water content profiles, was 7.4 μm with an image field of view (FOV) of 490 μm. A series of 1D profile were continuously acquired to temporally resolve the experiment, with a frame rate of one image every 610 s.

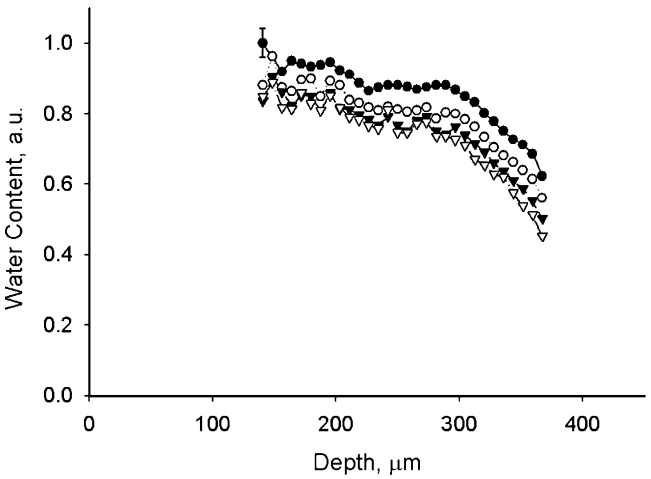

Fig. 2. 4 averaged water content profiles. Experiments (●), (○), (▼), (□) correspond to the average from the experimental time range of 0–3.4, 3.4–6.8, 6.8–10.2, 10.2–13.6 h. Water content uniformly decreased over 20 h, with a clear drying front observed at the drying side (right). The typical experimental uncertainty due to fitting is illustrated by the representative error bar in the top profile at the far left.

3. Results and discussions

3.1. Wetting and drying measurements

Unlike operating fuel cells, the mock fuel cell does not form a complete electrical circuit; it has no catalyst, no gas diffusion layers and no chemical reactions. The mock fuel cell does however provide well-controlled boundary conditions. The evolution of the water content across the Nafion membrane was investigated with a wetting/drying boundary condition.

As illustrated in Fig. 1, a water reservoir on the top of the Nafion layer was employed to maintain saturation and a dry gas flow underneath was employed for drying. In this case, we anticipate water flow into the top of the membrane to reach a steady state with drying from below. The wetting/drying experiment mimics possible operating conditions of a dry-gas-feed fuel cell in which the cathode is exposed to liquid water while the anode is relatively dry.

The experiment duration was approximately 20 h with more than 100 multi-echo profiles acquired, at approximately 10 min intervals [38]. The steady state lasted for approximately 18.5 h until the water reservoir emptied.

Fig. 2 reports 4 averaged water content profiles of this wetting/drying experiment. Each is averaged from the isolated water content profile of 20 measurements, which overall span 3.4 h. The water reservoir is at the left in the profiles with the drying chamber at right. It is hard to determine $\rho_0(y)$ at the profile edges, because the second or subsequent echo signals of these points are usually too small, which substantially complicates the data fitting. The Nafion sample is located from 140 μm to 360 μm, with the thickness approximately 220 μm.

The images clearly show a systematic variation in water content across the membrane. High water content shown on the wetting side (left) indicates a well maintained water content close to the wetting boundary. Moving from left to right, toward the drying side of the water content profile in Fig. 2, one observes an initially shallow decrease of water content. At a critical point in all the water content profiles, we observe a sharp decrease in water content moving toward the drying side.

Each of the four water content profiles of Fig. 2 is consistent with the bi-modal transport model, however they also exhibit an "aging" effect in which the water content decreases over many hours. This aging effect is quantified via systematic changes in the spatial resolution of the T_2 lifetime [38] and suggests a slow evolution of the microscopic Nafion port structure with a time constant of tens of hours, as suggested in the literature [47–51]. This aging effect implies that the threshold λ_t for the bi-modal transport model may depend upon quantities beyond the scope of our model, including the past history of the Nafion water concentration.

3.2. Numerical model

A medium with a uniform, isotropic microstructure, and a constant diffusivity, would predict a linear variation of water concentration between the two boundaries. This is in fact a classic hallmark of diffusion [52]. However, the nonlinear water distribution observed in our measurement suggests that a mechanism more complicated than simple diffusion is controlling the mass transport across the Nafion membrane.

3.2.1. Reduction of the Weber–Newman model

A key aspect of the wetting/drying data in Fig. 2 is the bi-modal nature of the water transport. Previous models for water transport in Nafion have proposed mechanisms for bi-modal and even tri-modal mechanisms. We focus on the model presented in [11,12] which combines transport models for vapor, vapor–liquid, and liquid equilibrated Nafion. The experimental data is consistent with a bi-modal subset of this model, incorporating the vapor and vapor–liquid transport mechanisms. In the absence of proton transport, the analysis below shows that the two-mode, Weber–Newman model is equivalent to a diffusive transport model in which diffusivity depends, sensitively, upon water volume fraction.

The Weber–Newman model is presented most succinctly in Eqs. (1.1)–(1.28) of [12], which we summarize below. Taking the transport to be entirely in the through-plane direction, x, and at equilibria, the vapor–liquid model prescribes the spatially constant ionic current, I, as

$$I = -S\left(\sigma_{11}\frac{d}{dx}\Phi + \sigma_{12}\frac{d}{dx}p_L\right) - (1-S)\left(\sigma_{21}\frac{d}{dx}\Phi + \sigma_{22}\frac{d}{dx}p_L\right) \quad (2)$$

where Φ is the electric potential and p_L is the liquid pressure, and S, the liquid saturation level, is an affine function of water content, λ,

$$S = \frac{\lambda - \lambda_V}{\lambda_L - \lambda_V} \tag{3}$$

In particular S increases from 0 to 1 as the water content varies from its saturated vapor level $\lambda = \lambda_V = \lambda_V(T)$ to the liquid level $\lambda = \lambda_L = 22$ waters/acid group. The water flux N is also spatially constant and is prescribed by

$$N = -S\left(\beta_{11}\frac{d}{dx}\Phi + \beta_{12}\frac{d}{dx}p_L\right) - (1-S)\left(\beta_{21}\frac{d}{dx}\Phi + \beta_{22}\frac{d}{dx}p_L\right), \tag{4}$$

where the dependence of the transport coefficients $\sigma_{ij}(\lambda, T)$ and $\beta_{ij}(\lambda, T)$ upon water content and temperature can be inferred from [12]. Moreover the liquid pressure is related to the saturation level via an empirical relation based upon assumptions of hydrophobicity ($\cos(\theta) < 0$) and a particular pore size distribution,

$$S = \frac{1}{2}\left(1 - erf\left(\frac{\ln[-(5/2)\gamma\cos(\theta)] - \ln p_L}{0.3\sqrt{2}}\right)\right) \tag{5}$$

This function is monotonic in $p_L > 0$, and hence may be inverted to slave the liquid pressure to the saturation level. However the saturation level in turn is a function of water density λ, which yields a capillary pressure relation,

$$p_L = p_L(\lambda), \tag{6}$$

for water fractions $\lambda \in [\lambda_V, \lambda_L]$, in the vapor–liquid regime.

In the wetting/drying experimental configuration, there is no ionic current, $I = 0$ in Eq. (2), so that the electric potential gradient must balance against the water pressure gradient,

$$\frac{d}{dx}\Phi = -\frac{S\sigma_{12} + (1-S)\sigma_{22}}{S\sigma_{11} + (1-S)\sigma_{22}}\frac{d}{dx}p_L. \tag{7}$$

Combining this expression with the dependence of the liquid pressure upon λ we may write the flux as

$$N = -D_{VL}(\lambda, T)\frac{d}{dx}\lambda, \tag{8}$$

where the effective diffusivity in the vapor–liquid regime, according to Eqs. (4) and (6), takes the form

$$D_{VL}(\lambda, T) = -\left(\frac{S\sigma_{12} + (1-S)\sigma_{22}}{S\sigma_{11} + (1-S)\sigma_{22}}(S\beta_{11} + (1-S)\beta_{21}) - (S\beta_{12} + (1-S)\beta_{22})\right)\frac{d}{d\lambda}p_L. \tag{9}$$

For water contents $\lambda < \lambda_V$, the liquid saturation S is considered to be zero, and the transport is determined from the gradient of the electric potential Φ and the chemical potential μ_0. The zero-current reduction slaves the electric potential and chemical potential gradients, and yields a simple flux relation of form

$$N = -\alpha_v(\lambda, T)\frac{d}{dx}\mu_0 = -D_V(\lambda, T)\frac{d}{dx}\lambda, \tag{10}$$

where the coefficient α_v is defined in Eq. (1.15) of [12] while the chemical potential can be viewed a function of λ and T [11], which motivates the definition of the effective vapor-equilibrated diffusivity, $D_V = \alpha_v\, d/d\lambda\, \mu_0$.

An unintuitive feature of the Weber–Newman model is that as λ decreases to the lower limit, λ_V, of the vapor–liquid regime, the vapor–liquid diffusivity D_{VL} not only increases but even becomes infinite. This fact is a direct consequence of the choice of the functional relation, Eq. (5), which leads to the corresponding capillary pressure relation, Eq. (6). Indeed, since $d/dp_L\, S$ approaches zero as S approaches zero, the inverse relation, $p_L = p_L(S)$, must obtain an infinite slope at $S = 0$. Equally, the derivative of the capillary pressure, which is a factor in the water diffusivity, satisfies $d/d\lambda\, p_L(\lambda_V) = \infty$. It seems more plausible, and is consistent with the data presented in Fig. 2, that the effective water diffusivity should increase monotonically with increasing water content, and indeed should increase rapidly with a transition of water content from the vapor to the vapor–liquid regimes, as illustrated in Fig. 3. To this end, and as is consistent with the level of resolution afforded by the data, we retain the dominant features of the Weber–Newman model, namely a bi-modal transport mechanism, Fig. 3, that shifts sensitively at the transitional water content, $\lambda = \lambda_V$, but simplify the flux relation to

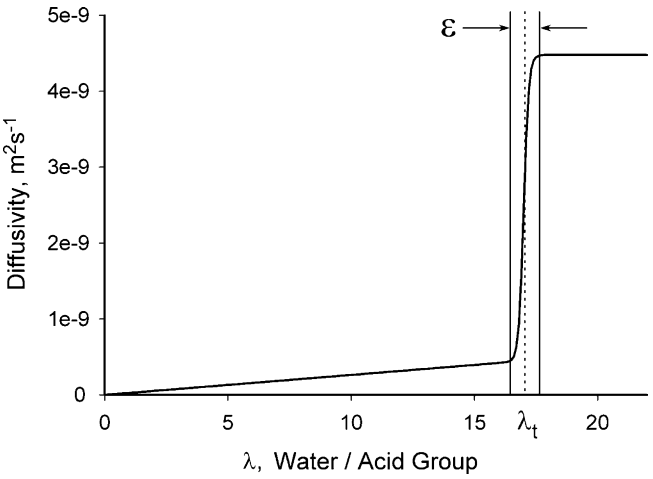

Fig. 3. "Bi-modal" diffusivity proposed as a function of water/acid group number. The threshold transition point is represented by λ_t, with the transition region represented by ε.

$$N = -D(\lambda)\frac{d}{dx}\lambda, \tag{11}$$

where the effective diffusivity, given by Eq. (4), is strictly increasing with water content, and exhibits a sharp transition from a linear dependence upon λ in the vapor regime, to a significantly higher constant value in the vapor–liquid regime at a transition value λ_t.

3.2.2. The minimal "bi-modal diffusivity" model

A schematic diagram of the numerical simulation is illustrated in Fig. 4, with the boundary conditions specified on the left and right sides. As the water transport problem considered in this study is only in the depth direction, possible mass transport along the membrane surface is neglected. The water concentration is denoted

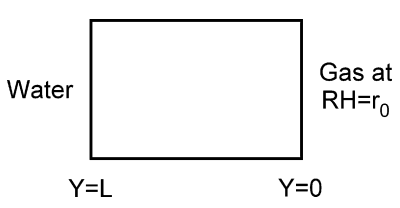

Fig. 4. A schematic diagram of the proposed mathematic model. The thickness of the sample is L, with the depth direction along Y direction, according to the axis system in Fig. 1. The drying boundary condition, represented by r_0, is listed at the right side of the sample diagram, with the wetting boundary condition, saturated water, listed at the left side.

by, $\lambda = \lambda(x)$, in dimensionless units of water/acid group. The actual water concentration is $a \cdot \lambda$, where a is the acid density, approximately 1200 moles m^{-3}.

Our minimal model is formulated as

$$\begin{cases} \dfrac{d}{dx}\left(D(\lambda)\cdot\dfrac{d\lambda}{dx}\right) = 0 \quad 0 < x < L \\ D(\lambda)\cdot\dfrac{d}{dx}\lambda(0) = +\gamma(\lambda(0) - \lambda_*(0)) \\ D(\lambda)\cdot\dfrac{d}{dx}\lambda(L) = -\gamma(\lambda(L) - \lambda_*(L)) \end{cases}, \tag{12}$$

where γ is the mass transport coefficient; D is the water diffusivity, which depends upon water content; $\lambda_*(RH)$ represent the equilibrium membrane water content as function of external RH, which is equivalent to the water vapor activity. Through an empirical formula, $\lambda_*(RH) = 0.043 + 17.81 \cdot RH - 39.85 \cdot RH^2 + 36 \cdot RH^3$ [53,54], $\lambda_*(RH)$ is calculated.

In our proposed "bi-modal" diffusivity model, Fig. 3, the diffusivity increases slowly in a linear manner from 0 water/acid number to λ_t, but jumps from a concentration near λ_t to a substantially higher value, when the concentration is greater than λ_t.

This diffusivity coefficient is described via the formulae,

$$\begin{cases} D = D_m \cdot \lambda \cdot H_m(\lambda) + D_p \cdot H_p(\lambda) \\ H_p(\lambda) = \dfrac{1 + \tanh((\lambda - \lambda_t)/\varepsilon)}{2}; \quad H_m(\lambda) = \dfrac{1 - \tanh((\lambda - \lambda_t)/\varepsilon)}{2} \end{cases}, \tag{13}$$

where ε controls the width of the diffusivity transition region, while D_m and D_p are constants calibrated to the data.

To resolve the model, Eq. (2), we observe that the flux $N = -a \cdot D(\lambda) \cdot d\lambda/dx$ is constant in space so that the model can be rearranged as,

$$\begin{cases} D(\lambda)\cdot\dfrac{d\lambda}{dx} = -\dfrac{N}{a} \\ \lambda(0) = \lambda_*(0) - \dfrac{N}{a\cdot\gamma} \\ \lambda(L) = \lambda_*(L) + \dfrac{N}{a\cdot\gamma} \end{cases}. \tag{14}$$

We introduce the cumulative function of the diffusivity, $\bar{D}(\lambda) = \int_0^\lambda D(\lambda)\cdot d\lambda$, so that $d/dx(\bar{D}(\lambda)) = -N/a$, and hence,

$$\bar{D}(\lambda) = \bar{D}_0 - \frac{N\cdot x}{a} \tag{15}$$

where $\bar{D}_0 = \bar{D}(\lambda(0))$ is an unknown constant. We solve for λ in terms of N, $\bar{D}_0$ as $\lambda = \bar{D}^{(-1)}(\bar{D}_0 - N\cdot x/a)$.

To determine the flux N, we interpret Eq. (15) from the boundary conditions and obtain, $\bar{D}(\lambda(L)) - \bar{D}(\lambda(0)) = -N\cdot L/a$. With the combination of Eqs. (12)–(14), a function of N is obtained,

$$\bar{D}\left(\lambda_*(L) + \frac{N}{a\cdot t}\right) - \bar{D}\left(\lambda_*(0) - \frac{N}{a\cdot t}\right) = -\frac{N\cdot L}{a} \tag{16}$$

One is therefore able to solve Eq. (16) for N through Newton's Method and determine $\bar{D}_0$ from the relation, $\bar{D}_0 = \bar{D}(\lambda(0)) = \bar{D}(\lambda_*(0) - N/a\cdot t)$.

3.2.3. Comparison of the model prediction with the experiment

We attribute the overall minor decrease of the water content profiles with time, Fig. 2, as being due to the slow micro-structural rearrangement of Nafion. Since this is a minor effect with a consistent shoulder structure among the four profiles, we average the four water content profiles to remove the transient aging behavior to yield steady-state experimental data, which can be used for comparison to model predictions, as illustrated in Fig. 5. The model curve, Fig. 5, is computed with the drying and wetting boundary conditions set as 0.12 and 1 according to the RH of the dry air flow and the water.

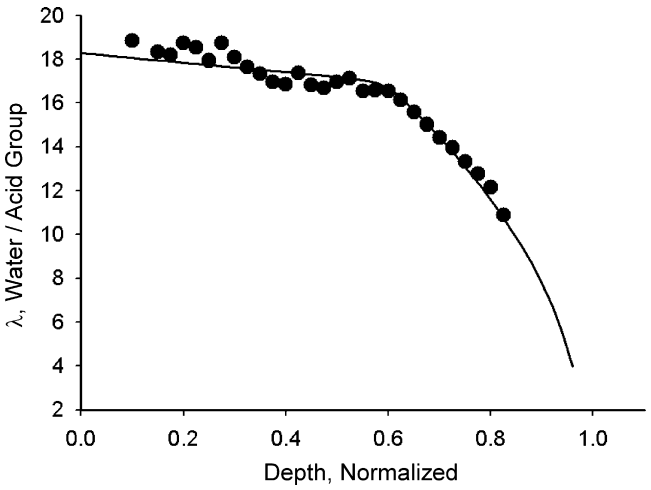

Fig. 5. Comparison of the computed model curve (–) against the wetting/drying experimental data (●), an average of the four profiles shown in Fig. 2. A satisfying match is observed which demonstrates the correctness of the proposition of a bi-modal diffusivity.

The difficulty of proper T_2 fitting of the edges of the T_2-weighted profiles yields an incomplete water content profile. As a result the two edges of the profile are not matched to the boundary conditions. Hence, in this study the experimental water profile is slightly rescaled to make the end points correspond to two empirically estimated RH values. Since this change does not affect the pattern of water distribution and the inherent variation of diffusivity, the compatibility of the proposed model with the experimental data is therefore maintained.

Our transition value, $\lambda_t = 16$ at $T = 20\,^\circ$C, is in excellent agreement with the Weber–Newman value of λ_V for an unconstrained membrane, as extrapolated from the data presented in Fig. 3 of Ref. [12]. Moreover, the satisfying match of the model prediction and experiment observed in Fig. 5 supports our basic assumption of a bi-modal diffusivity. In addition, this match indicates the existence of a critical water concentration where a dramatic change in diffusion occurs, which also suggests a threshold may exist across the Nafion in an operating fuel cell.

To our knowledge, this experimental data afford the first direct observation of such a nonlinear water distribution through a Nafion membrane due entirely to water transport. The possible underpinning mechanisms are a matter of speculation at this time. A possible mechanism could include a phase transition in the water pore network that may occur at a critical water volume fraction, which in turn engenders a shift in either diffusivity or permeability. A full characterization of the nature of water transport and water network re-organization is the subject of ongoing work.

4. Conclusion

This paper describes measurement of the water content variation across a Nafion membrane inside a mock fuel cell, under a wetting/drying boundary condition. The water content profiles of the wetting/drying measurement present a behavior that is inconsistent with uniform mass transport in Nafion. A minimal mathematic model, with an assumption of a bi-modal water transport mechanism made from a reduced Weber–Newman model, is constructed according to the experimental observations, with the subsequent model predictions providing excellent match to the data.

Measurements of this type show the great potential of ex situ characterization of water management related properties of Nafion, under a wide variety of conditions, i.e. temperature, pressure, hydration, and mechanical stress, on water transport across the membrane. To obtain absolute water content imaging, one could calibrate image intensity of the resultant images by simultaneously measuring an isolated yet closely positioned, saturated Nafion layer with known water content as reference. In addition, the techniques employed in this study can be translated to measurement in operational PEM fuel cells.

Acknowledgements

B.J.B. thanks NSERC of Canada for operating and equipment grants. B.J.B. also thanks the Canada Chairs program for a Research Chair in MRI of Materials (2002–2016). K.P. would like to thank the NSF DMS 0708804. We thank R.P. MacGregor for his assistance with the experiments and M. Olive and B. Titus for fabricating the sample holder and RF probe.

References

[1] W. Vielstich, H.A. Gasteiger, A. Lamm, Handbook of Fuel Cell – Fundamentals, Technology and Applications, John Wiley & Sons, 2003.
[2] R.A. Lemons, J. Power Sources 29 (1990) 251–264.
[3] G. Hoogers, Fuel Cell Technology Handbook, CRC Press, New York, 2000.
[4] T.E. Springer, T.A. Zawodzinski, S. Gottesfeld, J. Electrochem. Soc. 138 (1991) 2334–2342.
[5] T.A. Zawodzinski, C. Derouin, S. Radzinski, R.J. Sherman, V.T. Smith, T.E. Springer, J. Electrochem. Soc. 140 (1993) 1041–1047.
[6] M. Eikerling, Y. Kharkats, A. Kornyshev, Y. Volfkovich, J. Electrochem. Soc. 145 (1998) 2684–2699.
[7] G.J. Janssen, J. Electrochem. Soc. 148 (2001) 1313–1323.
[8] P.A.C. Chang, G.S. Kim, K. Promislow, B. Wetton, J. Comp. Phys. 223 (2007) 797–821.
[9] K. Promislow, P. Chang, H. Haas, B. Wetton, J. Electrochem. Soc. 155 (7) (2008) A494–A504.
[10] I. Nazarov, K. Promislow, J. Electrochem. Soc. 154 (7) (2007) B623–630.
[11] A. Weber, J. Newman, J. Electrochem. Soc. 151 (2) (2004) A316–339.
[12] A. Weber, J. Newman, AIChE J. 50 (12) (2004) 3215–3226.
[13] M. Dresselhaus, G. Crabtree, M. Buchanan, Basic Research Needs for the Hydrogen Economy: Report on the Basic Energy Sciences Workshop on Hydrogen Production, Storage, and Use, Department of Energy, 2003.
[14] J. St-Pierre, J. Electrochem. Soc. 154 (7) (2007) B724–B731.
[15] K.A. Mauritz, R.B. Moore, Chem. Rev. 104 (2004) 4535–4585.
[16] M. Rankothge, G. Haryadi, J. Moran, L. Hook, Van Gorkom, Solid State Ionics 67 (1994) 241–248.
[17] H. Chen, G.R. Palmese, Y.A. Elabd, Chem. Mater. 18 (2006) 4875–4881.
[18] R.T. Baker, L. Naji, K. Lochhead, J.A. Chudek, Chem. Commun. (2003) 962–963.
[19] K. Tüber, D. Pócza, C. hebling, J. Power Sources 124 (2003) 403–414.
[20] X.G. Yang, F.Y. Zhang, A.L. Lubawy, C.Y. Wang, Electrochem. Solid-State Lett. 7 (2004) A408–A411.
[21] K. Sugiura, M. Nakata, T. Yodo, Y. Nishiguchi, M. Yamauchi, Y. Itoh, J. Power Sources 145 (2005) 526–533.
[22] X. Liu, H. Guo, C. Ma, J. Power Sources 156 (2006) 267–280.
[23] Y. Ishikawa, T. Morita, K. Nakata, K. Yoshida, M. Shiozawa, J. Power Sources 163 (2007) 708–712.
[24] R. Mosdale, G. Gebel, M. Pineri, J. Membr. Sci. 118 (1996) 269–277.
[25] R.J. Bellows, M.Y. Lin, M. Arif, A.K. Thompson, D. Jacobson, J. Electrochem. Soc. 146 (1999) 1099–1103.
[26] R. Satjia, D.L. Jacobson, M. Arif, S.A. Werner, J. Power Sources 129 (2004) 238–245.
[27] D. Kramer, J. Zhang, R. Shimoi, E. Lehmann, A. Wokaun, K. Shinohara, G.G. Sherer, Electrochim. Acta 50 (2005) 2603–2614.
[28] M.A. Hickner, N.P. Siegel, K.S. Chen, D.N. McBrayer, D.S. Hussey, K.L. Jacobson, M. Aril, J. Electrochem. Soc. 153 (2006) A902–A908.
[29] J.J. Kowal, A. Turhan, K. Heller, J. Brenizer, M.M. Mench, J. Electrochem. Soc. 153 (2006) A1971–A1978.
[30] K. Teranishi, S. Tsushima, S. Hirai, Therm. Sci. Eng. 10 (2002) 59–60.
[31] K.W. Feindel, L.P. LaRocque, D. Starke, S.H. Bergens, R.E. Wasylishen, J. Am. Chem. Soc. 126 (2004) 11436–11437.
[32] S. Tsushima, K. Teranishi, S. Hirai, Energy 30 (2005) 235–245.
[33] K.R. Minard, V.V. Viswanathan, P.D. Majors, L.Q. Wang, P.C. Rieke, J. Power Sources 161 (2006) 856–863.
[34] K.W. Feindel, S.H. Bergens, R.E. Wasylischen, J. Am. Chem. Soc. 128 (2006) 14192–14199.
[35] P.J. McDonald, Prog. Nucl. Magn. Reson. Spectrosc. 30 (1997) 69–99.
[36] P.M. Glover, P.J. McDonald, B. Newling, J. Magn. Reson. 126 (1997) 207–212.
[37] A.V. Ouriadov, R.P. MacGregor, B.J. Balcom, J. Magn. Reson. 169 (2004) 174–186.
[38] Z. Zhang, A.E. Marble, B. MacMillan, K. Promislow, J. Martin, H. Wang, B.J. Balcom, J. Magn. Reson. 194 (2008) 245–253.
[39] Z. Zhang, J. Martin, J. Wu, H. Wang, K. Promislow, B.J. Balcom, J. Magn. Reson. 193 (2008) 259–266.
[40] K. Promislow, B. Wetton, SIAM Appl. Math. 70 (2009) 369–409.
[41] M.W. Verbrugge, R.F. Hill, J. Electrochem. Soc. 137 (1990) 886–893.
[42] D.M. Bernardi, M.W. Verbrugge, AIChE J. 37 (1991) 1151–1163.
[43] N.H. Jalani, P. Choi, R. Datta, J. Mem. Sci. 254 (2005) 31–38.
[44] R.B. Moore III, C.R. Martin, Macromolecules 21 (1988) 1334–1339.
[45] B.J. Balcom, R.P. MacGregor, S.D. Beyea, D.P. Green, R.L. Armstrong, T.W. Bremner, J. Magn. Reson. 123 (1996) 131–134.
[46] S. Gravina, D.G. Cory, J. Magn. Reson. B 104 (1994) 53–61.
[47] G. Gebel, Polymer 41 (2000) 5829–5838.
[48] V. Barbi, S.S. Funari, R. Gehrke, N. Scharnagl, N. Stribeck, Polymer 44 (2003) 4853–4861.
[49] W. Essafi, G. Gebel, R. Mercier, Macromolecules 37 (2004) 1431–1440.
[50] M.H. Kim, C.J. Glinka, S.A. Grot, W.G. Grot, Macromolecules 39 (2006) 4775–4787.
[51] L. Rubatat, O. Diat, Macromolecules 40 (2007) 9455–9462.
[52] F.P. Incropera, D.P. DeWitt, Fundamentals of Heat and Mass Transfer, 5th ed., John Wiley & Sons, 2002.
[53] I. Nazarov, K. Promislow, J. Electrochem. Soc. 154 (7) (2007) B623–B630.
[54] J.T. Hinatsu, M. Mizuhata, H. Takenaka, J. Electrochem. Soc. 141–6 (1994) 1493–1498.